

pubs.acs.org/Macromolecules Article

Polymerization of Free-Volume-Promoting Monomers for Methane Absorption

Haosheng Feng, Shao-Xiong Lennon Luo, and Timothy M. Swager*



Cite This: *Macromolecules* 2024, 57, 7533–7546



Read Online

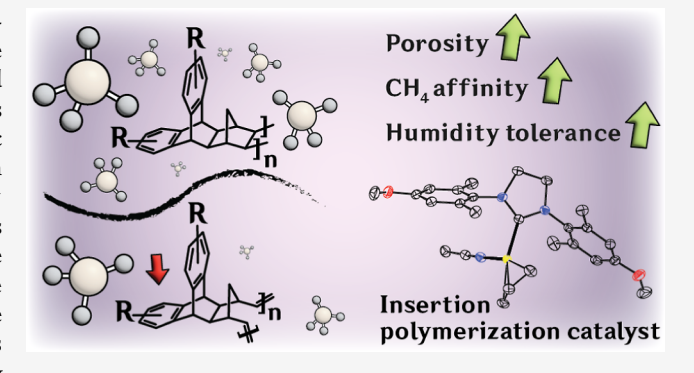
ACCESS I

Metrics & More

Article Recommendations

Supporting Information

ABSTRACT: Cationic palladium catalysts containing *N*-heterocyclic carbene ligands were found to be effective catalysts for the chain-growth polymerization of monomers based on a fused [2.2.1]:[2.2.2] ring system. The shape-persistent monomers prevent dense packing of polymer chains and produce intrinsic microporosity in polymer solids. Gas absorption isotherm measurements reveal that surface areas greater than 1000 m² g⁻¹ are produced in some materials. High molecular weight materials are produced, and catalyst optimization studies reveal that the steric bulk and electronic nature of the *N*-heterocyclic carbene ligands play dominant roles in determining the efficiency of the polymerization. The hydrocarbon nature of the microporous polymers enables methane absorption even at high humidity levels which has anticipated utility in the greation of concentrates.



levels, which has anticipated utility in the creation of concentrators for robust point methane sensors.

■ INTRODUCTION

Methane (CH₄) is the major component in natural gas¹ and is a widely used energy source as a result of its cleaner combustion and higher energy content relative to other fossil fuels such as oil and coal.^{2,3} Unfortunately, in addition to posing an explosive risk at elevated concentrations,⁴ methane is also a potent greenhouse gas with a 20 year global warming potential that is 82.5 times higher than carbon dioxide.⁵ As a result, there is a need for expanded methane monitoring and abatement.^{6–9}

There are multiple methods for monitoring methane and detecting its release into the environment. Satellites can image larger emissions on a global scale, 10,11 but point detection devices are more suitable on smaller scales for distributed trace detection at places of interest. The latter implementation is attractive as it allows the identification of a more precise location of the leakage source. Most point-sensing devices make use of calorimetry, 12 chemiresistive responses from metal oxide semiconductors, 13-15 and electrochemical oxidation. 16,17 To be cost-effective as distributed sensors, devices need to have low power consumption, be inexpensive, exhibit minimal off-target interference, and be operable over a range of temperature and humidity levels. There have been multiple reviews on the development of methane sensors, 18-20 but trace methane detection is generally limited to elevated temperatures,²¹ which makes for high energy consumption. Other factors such as temperature, humidity, and cross sensitivity to interferants also negatively impact device performance.²⁰ Our lab has reported a chemiresistive methane-sensing system based on carbon nanotubes and a platinum catalytic methane oxidation cycle that operates at room temperature. It also showed

selectivity for methane over other hydrocarbons.²² Unfortunately, this system's performance is compromised at high humidity, with negligible responses measured at humidity levels exceeding 40%.

To create more robust methane sensors, we have been interested in creating hydrophobic polymers that will absorb methane over a wide range of humidity. These materials have utility as selective membranes that block humidity but can transport methane to the sensor. Alternatively, an absorbing polymer could be used as a preconcentrator that selectively captures methane for thermal release to a proximate sensor. The latter method enables temporal sequencing, which produces a more robust signal that can be used to differentiate between noise and analyte responses. Similar approaches have been used to improve sensor performance for H_2 , 23 H_2 S, 24 as well as other volatile organic compounds.²⁵ To optimally implement either of these methods, it is important to maximize a polymer's affinity for methane over interferents (humidity). Intrinsically porous structures ensure that a material can both absorb methane without undue swelling and also facilitate diffusion. Metal organic frameworks have been used as preconcentrators; 26,27 however, these materials have electronegative atoms in the

Received: May 10, 2024 Revised: June 28, 2024 Accepted: July 3, 2024 Published: July 18, 2024





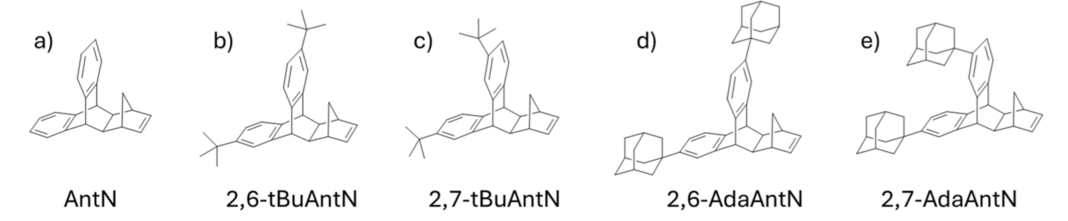


Figure 1. Structures of monomers examined in this study.

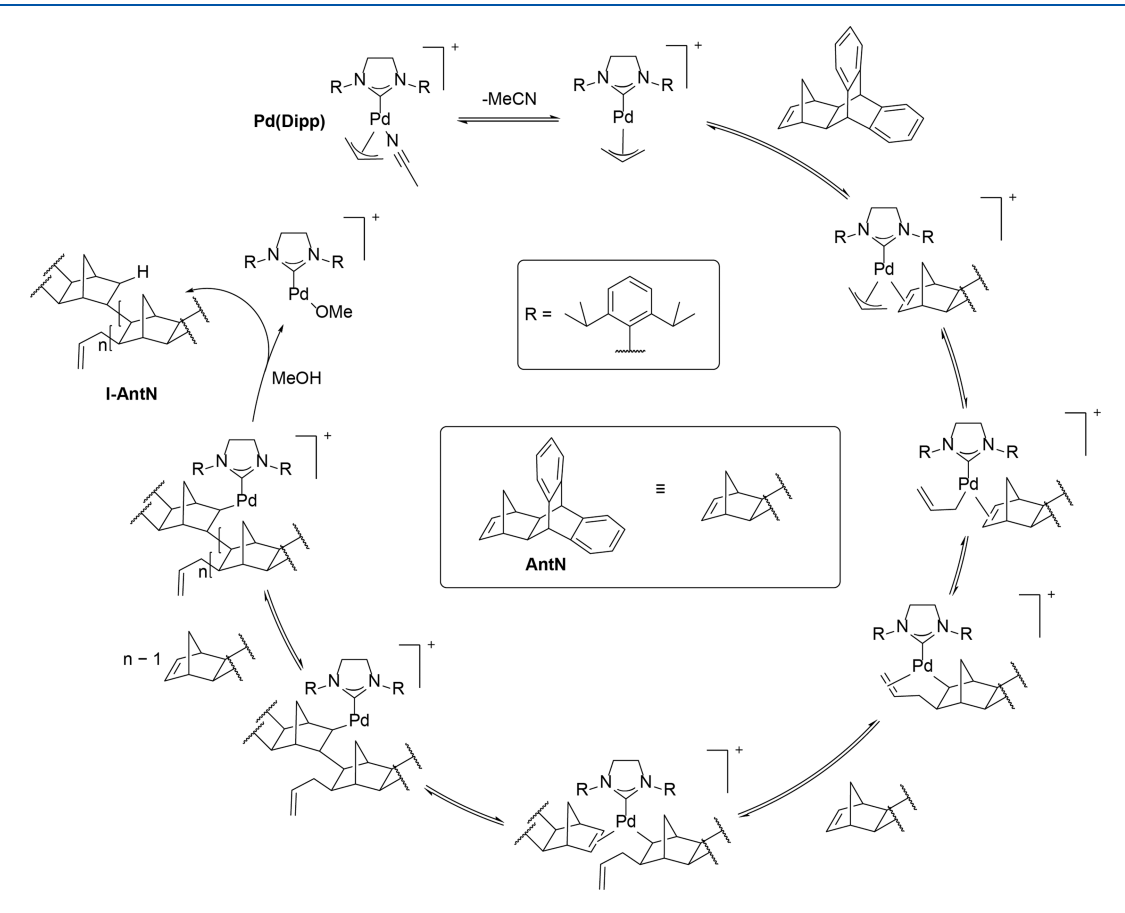


Figure 2. Mechanistic scheme for Pd-catalyzed insertion polymerization of norbornenes, using Pd(Dipp) and AntN as illustration.

ligands and electropositive metals and the associated polarization results in water absorption as well. To meet the required characteristics of a humidity-independent methane absorption, we have designed porous hydrocarbon polymers that lack heteroatoms and their associated dipolar elements. In this regard, we have identified rigid 3-D [2.2.1] bicyclic norbornane hydrocarbon structures that with an insertion polymerization retain the full rigid 3D structure after polymerization, thereby improving porosity. Related work by Finkelshtein and coworkers have also shown that introducing bulky silyl²⁸ and siloxy²⁹ groups onto these rigid frameworks gives highly permeable polymers with good gas-separation properties. In our case, the fusion of triptycene groups to the polymer backbone faithfully produces polymers with intrinsic porosity.³⁰ We have also found that [2.2.1] bicyclic structures, such as the norbornane groups retained within the polymer, similarly produce high porosity when fused to the polymer backbone.³¹ In this investigation, we also make use of chain growth insertion polymerization to produce high molecular weights and enable the prospect to create block polymer structures. An added

element of our design is that monomers are produced in one or two steps from abundant, inexpensive starting materials.

In accordance with our goals, we report herein the synthesis of several norbornene monomers (Figure 1) bearing fused [2.2.1]: [2.2.2] bicyclic rings. The insertion polymerization was optimized, and methane affinity was determined using quartz crystal microbalance (QCM) measurements. We also demonstrate that retaining the norbornane framework through an insertion provides superior methane affinity relative to compositionally equivalent polymers produced from ring-opening metathesis polymerization (ROMP).

■ RESULTS AND DISCUSSION

Norbornene is a key building block with the requisite strained alkene for polymerization and lacks polar groups that attract water molecules. Polymerization of norbornene has been extensively reviewed³² and includes (1) insertion (addition) polymerization,^{33–37} (2) ROMP,^{38–41} and (3) catalytic arenenorbornene annulation (CANAL) polymerizations.^{42,43} Insertion polymerizations are ideal for the norbornene system as a

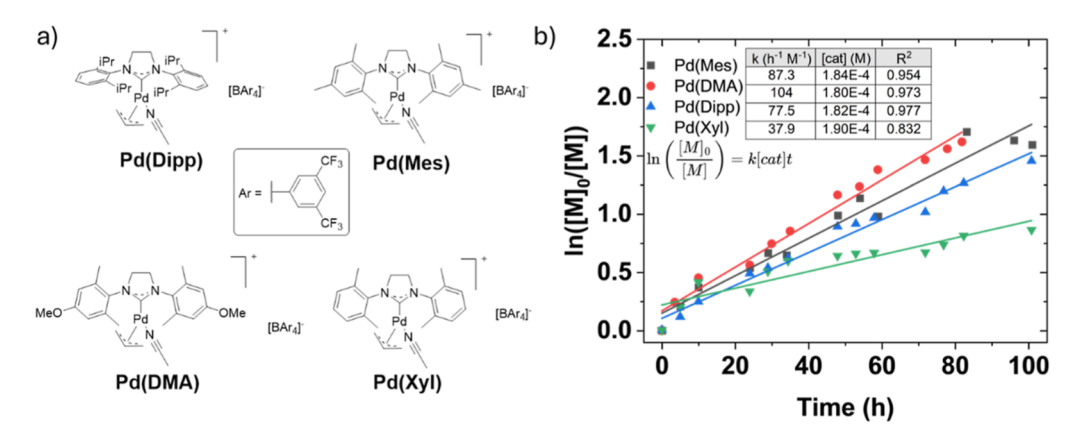


Figure 3. (a) Structures of Pd catalysts examined in this study. (b) Polymerization kinetics of 2,6-tBuAntN using these four catalysts.

Scheme 1. (a) Synthesis of 2,6-tBuAnt and 2,7-tBuAnt; (b) Synthesis of 2,6-AdaAnt and 2,7-AdaAnt; and (c) Diels—Alder Reaction between Norbornadiene and Substituted Anthracenes to Give the Four Monomers 2,6-tBuAntN, 2,7-tBuAntN, 2,6-AdaAntN, and 2,7-AdaAntN

result of the fact that the syn-stereochemistry of each insertion reaction and the inability to produce a bridgehead double bond (Brett's rule) prevent β -hydride elimination reactions that complicate metal insertion polymerizations of acyclic alkenes. Additionally, an insertion mechanism preserves the rigid [2.2.1] bicyclic structure, which generates free volume and intrinsic porosity. To enhance the porosity generated by the norbornene, we took inspiration from triptycene, which robustly promotes internal free volume. 44-46 As part of an earlier study directed at determining a general design rule to create polymers with intrinsic microporosity, we found that ROMP of benzonorbornenes with fused triptycenes produced polymers with low dielectric constants and surface areas of 400 m² g⁻¹.⁴⁴ Our target fused [2.2.1]:[2.2.2] monomers can be easily synthesized by Diels-Alder reactions of anthracenes with norbornadiene. Adamantyl and t-butyl (tBu) substituents were added to anthracene via acid-catalyzed electrophilic aromatic substitution to enhance the solubility and physical size of the 3-D structures in the polymers. The parent monomer (AntN) has been utilized in the literature to synthesize a copolymer with ethene using insertion polymerization, ⁴⁷ but its successful insertion polymerization into the homopolymer was only very recently reported. ⁴⁸

During the initial catalyst screening, we were pleased that the simplest catalyst $[Pd(MeCN)_4][BF_4]_2$, first reported to polymerize norbornene, 33 was also competent in polymerizing AntN, giving a material (I-Ant) highly soluble in THF with a molecular weight of 22 kDa determined by gel permeation chromatography (GPC) (Figure S1a). Even more promising was that the $\rm N_2$ Brunauer–Emmett–Teller (BET) surface area of the polymer powder was 589 m² g $^{-1}$ (Figure S1b). Based on this result, we anticipated that utilizing more active catalysts could further improve molecular weight as well as surface areas. To this end, we have focused on N-heterocyclic carbene palladium catalysts previously reported in the literature that are air stable and enable polymerization under ambient atmosphere. 49

Initial attempts with the more readily accessible catalyst Pd(Dipp) (Figure 3a) gave an insoluble precipitate during polymerization of AntN presumably as a result of the higher molecular weight of the polymers. Zotkin et al. also reported obtaining insoluble material when using a Pd(OAc)₂-based

Scheme 2. One-Pot Syntheses of Imidazolium Chloride Precursors

catalyst for polymerizing AntN. 48 These insoluble powders showed enhanced BET surface areas of 838 m² g⁻¹ (Figure S1b), illustrating the value of producing higher molecular weight materials. As a result, we were hopeful that the more sterically bulky monomers, 2,6-tBuAntN and 2,7-tBuAntN (Figure 1b,c), would improve solubility at higher molecular weights. The substituted anthracenes were readily synthesized on scale under simple electrophilic aromatic substitution conditions, using anthracene and tert-butyl chloride with good yield under ambient atmosphere with reagent-grade solvents. A mixture of 2,6-tBuAnt and 2,7-tBuAnt was obtained that was separated effectively via slow crystallization from hexanes (Scheme 1a). The adamantyl anthracenes (2,6-AdaAnt and 2,7-AdaAnt) were also prepared by electrophilic substitution reactions to anthracene (Scheme 1b). A final Diels-Alder reaction between the four substituted anthracenes and excess norbornadiene affords the desired monomers as a racemic mixture, which were purified by filtration through a plug of silica gel (Scheme 1c). Only Diels-Alder products corresponding to cycloaddition to the norbornadiene's exo face were observed. Traditional assignment of the reaction as endo or exo with respect to the diene (anthracene) is ambiguous (Scheme S1). Polymerizing **2,6-tBuAntN** with Pd(Dipp) gave a polymer with $M_p = 38$ kDa that remained highly soluble in THF (Figure S1a). Attempts to polymerize 2,6-tBuAntN with [Pd(MeCN)₄][BF₄] under identical conditions as AntN did not lead to significant conversion, suggesting that the bulkier monomer requires a more active polymerization catalyst. Based on 2,6-tBuAntN's good performance as a monomer and the solubility of its polymers, we used this system for catalyst optimization studies. The polymerization of **AntN** with **Pd(Dipp)** is detailed with the accepted mechanism in Figure 2.49

A previous study compared the insertion polymerization kinetics of Pd(Dipp) and Pd(Mes) and determined the latter to display a higher rate of monomer consumption during polymerization of substituted norbornenes.⁴⁹ The authors attributed this to Pd(Mes) having a less hindered N-heterocyclic carbene (NHC),50 and we hypothesized that an electrondonating substituent in the para-position may be beneficial by enhancing the ligand affinity to the Pd. Therefore, we synthesized Pd(Xyl) as well as Pd(DMA) (Figure 3) to evaluate the influence of para-electron-donating substituents. The dihydroimidazolium chloride precursors (2a and 2b) are readily synthesized in a one-pot reaction by modification of procedures reported by Kuhn and Grubbs (Scheme 2).⁵¹ Separation of 2a and 2b from their respective formamidine chlorides (3a and 3b) is achieved by Soxhlet extraction (see the Supporting Information). Subsequent metalation⁵² with allylpalladium(II) chloride dimer and anion exchange⁴⁹ with tetrakis(3,5-bis-(trifluoromethyl)phenyl)borate were also performed following literature procedures.

With four catalysts in hand (Figure 3a), we then measured their polymerization rates of 2,6-tBuAntN by 1H NMR using 1,3,5-trimethoxybenzene as an internal standard (see the Supporting Information). Monomer consumption was tracked by the decrease in the norbornene alkene signal at 6.13 ppm, with results shown in Figure 3b. Consistent with a well-behaved chain growth polymerization, monomer consumption was linear over time and the polymerizations display first-order monomer dependence. Pd(Mes) displayed a higher rate of monomer consumption relative to Pd(Dipp), which is consistent with prior reports. 49

Kinetic measurement comparisons of Pd(Mes), Pd(Xyl), and Pd(DMA) indicate that the electron-donating methoxy group in Pd(DMA) gives a higher rate of polymerization and therefore all subsequent polymerizations were carried out with Pd(DMA) unless otherwise stated. The higher catalytic activity is also found to generate polymers with higher M_n in excess of 10^6 Da. This result is evident from the evolution of GPC chromatograms over time for the four different catalysts (Figure S5 and Table 1).

Table 1. Polymerization Results from Catalyst Optimization Using 2,6-tBuAnt \mathbf{N}^b

catalyst	$(h^{-1}M^{-1})$	$M_{ m n}$	PDI	total monomer consumption (%)
Pd(Dipp)	77.5	5.0×10^{5}	1.9	44
Pd(Mes) ^a	87.3	8.8×10^{5}	2.0	48
Pd(DMA) ^a	104	1.5×10^{6}	2.0	56
Pd(Xyl)	37.9	2.5×10^{4}	2.2	17

^aBimodal distribution observed on GPC. Reported values correspond to the higher molecular weight population. ^bReaction conditions: air, DCM, 0.14 mol % catalyst at $28 \, ^{\circ}\text{C}$.

It appears that concurrently increasing the electron density on the aromatic ring and reducing the steric bulk at the orthopositions (Me vs i-Pr) of NHC ligand give an optimal catalyst. Unexpectedly, Pd(Xyl) showed rapid deactivation during polymerization, as illustrated by a lower rate constant and R^2 value in the kinetic analysis. We found that this catalyst is prone to decomposition to give back solids when dissolved in less-coordinating solvents such as DCM and toluene. Hence, reduced steric bulk at the ortho-positions needs to be accompanied by para-donor substitution to maintain the catalyst stability.

Despite Pd(Xyl)'s instability, we successfully obtained single crystals suitable for X-ray diffraction studies of this catalyst and Pd(DMA) (Figure 4). There are no significant differences in the Pd-NHC bond length between Pd(Dipp) and Pd(Mes) (Table 2). However, the Pd-NCMe bond lengths were slightly longer in both Pd(Dipp) and Pd(Xyl). The lower solution stability of Pd(Xyl) may be caused by a labile MeCN ligand compounded by the lower degree of steric protection relative to

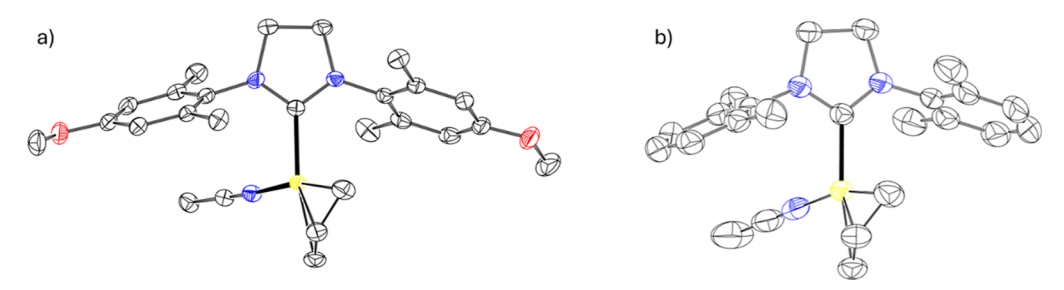


Figure 4. Single crystal structures of Pd(DMA) and Pd(Xyl). Ellipsoids shown at 50% probability. Anion and disorder excluded for clarity. Pd-N bond lengths (Å) are 2.0645(17) and 2.075(6), while Pd-NHC bond lengths are 2.0435(18) and 2.048(3), respectively.

Table 2. Selected Bond Lengths in the Crystal Structure of Catalysts

bond lengths (Å)	Pd(Dipp) (cinn) ^a	Pd(Mes) ^b	Pd(Xyl)	Pd(DMA)
Pd-NHC	2.048(6)	2.043(8)	2.048(3)	2.0435(18)
Pd-NCMe	2.077(4)	2.059(9)	2.075(6)	2.0645(17)

^aFrom ref 49. A cinnamyl anion is coordinated to Pd rather than an allyl anion. ^bFrom ref 49.

the isopropyl groups in Pd(Dipp). Lastly, the best performing catalyst, Pd(DMA), has a strong Pd-NHC interaction similar to that of Pd(Mes), but the donation from the *para*-methoxy group can result in greater lability in the MeCN ligand.

We also compared the polymerization kinetics of AntN relative to those of **2,6-tBuAntN** when using Pd(DMA). The former displayed a roughly 60 times larger rate constant, and monomer consumption was complete within 10 h, whereas the latter had only reached 60% monomer consumption after 3 days (Figure 5). The slower polymerization kinetics with the *t*Bu groups on the monomer are likely the result of crowding around the Pd catalytic center caused by the growing polymer chain. The rate constants for both **2,6-** and **2,7-tBuAntN** were similar (Figure 5b), suggesting that the norbornene reactivity is not significantly altered by the different substitution patterns. However, the chromatogram of the **2,7-tBuAntN** polymer displayed reduction of the high molecular weight components (Figure S6).

The monomers bearing adamantyl groups (2,6-AdaAntN and 2,7-AdaAntN, Figure 1d,e) were explored and their larger size relative to *t*Bu was expected to increase the porosity of the resultant polymer. The crystal structure and mass spectrogram of 2,6-AdaAnt were reported previously;⁵³ however, the

synthesis was only described in the patent literature along with 2.7-AdaAnt. 54

The X-ray structures (Figure 6) of the monomers reveal similar bond lengths of the strained alkenes (1.312–1.336 Å) to

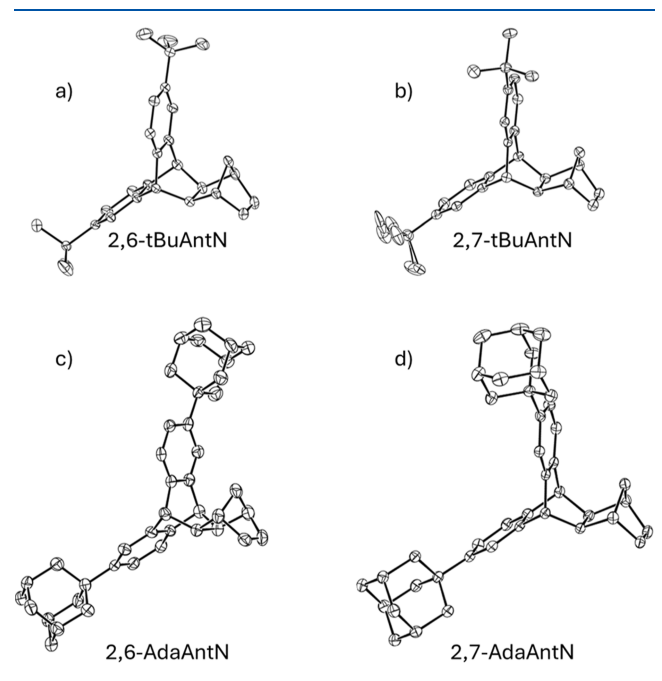
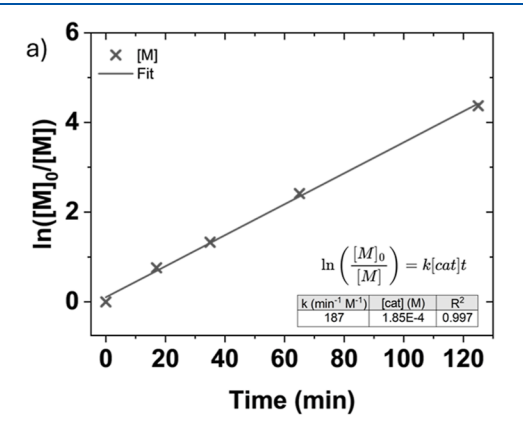


Figure 6. Single-crystal structures of (a) **2,6-tBuAntN**, (b) **2,7-tBuAntN**, (c) **2,6-AdaAntN**, and (d) **2,7-AdaAntN**. Ellipsoids are shown at 50% probability level. Norbornene C=C bond lengths are 1.326(4), 1.325(4), 1.312(9), and 1.336(5) Å, respectively.



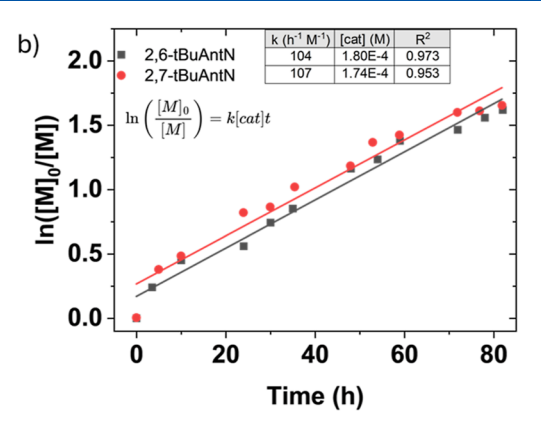


Figure 5. Polymerization kinetics of (a) AntN and (b) two isomers of tBuAntN using Pd(DMA) as the catalyst.

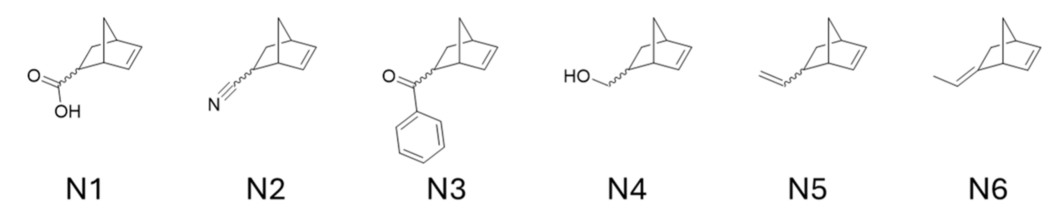


Figure 7. Monomers (endo- and exo mixtures) tested for polymerization with Pd(Mes) to see if any gives a bimodal GPC chromatogram.

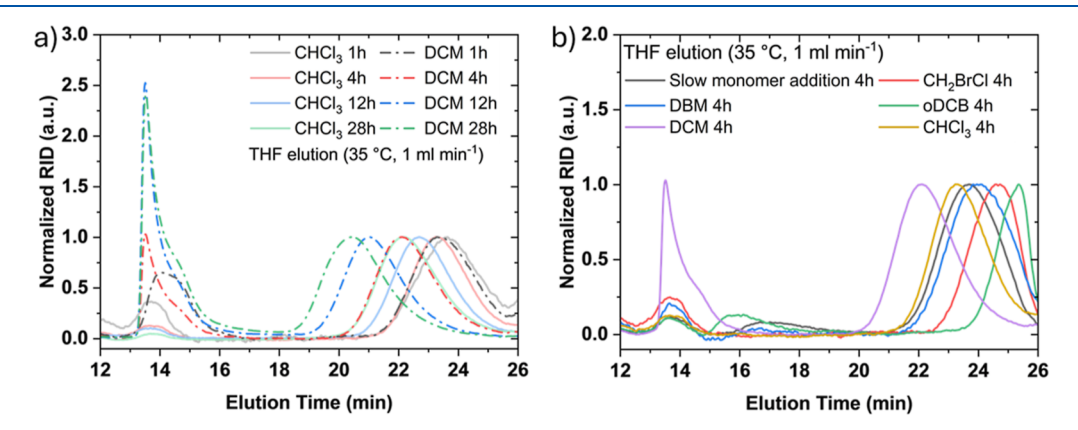


Figure 8. GPC chromatograms for addition polymerization of 2,6-tBuAntN with Pd(DMA) in different solvents. (a) CHCl₃ and DCM sampled at several time points. (b) Comparison of different solvents on polymerization after 4 h. GPC artifacts are visible between 12 and 14 min in both plots.

other norbornenes, ^{55–58} suggesting that the substituents do not significantly change the strain in the double bond. Unfortunately, both **AdaAntN** monomers were significantly less soluble than their *tert*-butyl counterparts in THF, DCM, and CHCl₃ solvents. As a result, none of the Pd catalysts examined were able to produce polymeric **AdaAntN** materials with molecular weights over 10 kDa (Figure S7). Considering the similar norbornene C=C bond lengths in the monomers, we postulate that the bulkier adamantyl substituents and low solubility hinder polymerization. In accord with these considerations, the rate of monomer consumption was lower than that observed for **2,6** and **2,7-tBuAntN**.

Chlorinated solvents such as DCM and $CHCl_3$ are not ideal for a sustainable synthesis; as a result, we explored more environmentally benign solvents such as THF and 2-MeTHF in the polymerizations. Unfortunately, no polymer was observed using Pd(DMA) in either THF or 2-MeTHF, even with the most reactive monomer AntN. Apparently, the cationic Pd center is deactivated by ether coordination, and generating the required alkene binding event to a vacant coordination site prior to insertion is not possible under these conditions. We also observed that the ethereal reaction mixture is colorless, as opposed to pale yellow observed with halogenated solvents. This observation is consistent with a different coordination environment around Pd in the two solvent classes.

We did have limited success with Pd(Dipp) as the catalyst in 2-MeTHF and partial conversion of AntN to polymer was observed via precipitation of the insoluble polymer material. However, the more coordinating THF prevented polymerization under the same conditions. This result does suggest that balancing the larger steric bulk provided by the *i*-Pr groups in the ligands with a bulkier ethereal solvent can be effective in facilitating polymerization. Unfortunately, GPC analysis of the polymer produced in 2-MeTHF is not possible due to poor solubility and qualitative observations for different reaction conditions tested are summarized in Table S1.

During the course of catalyst optimization, analysis of the crude (unfractionated) polymers of **2,6-tBuAntN** produced with **Pd(DMA)** and **Pd(Mes)** revealed unexpected bimodal distributions in the chromatograms (Figure S5). Polymers produced with these catalysts display chromatograms with a lower molecular weight material ($t \approx 20$ min retention time) and a distinctly non-Gaussian peak at lower elution time (t = 15 min) that is estimated to have a molecular weight exceeding 10^6 Da. This $M_{\rm n}$ is much higher than the theoretical expected value using 0.14 mol % of the catalyst that should give a degree of polymerization of 700 (2.7×10^5 Da for **2,6-tBuAntN**, M.W. = 383). We endeavored to understand the factors contributing to the formation of the bimodal distribution and high molecular weight fraction.

The polymerization reactions only involve three components (catalyst, monomer, and solvent). We have also shown that changing the catalyst can eliminate the high molecular weight fraction. As a result, we examined the role of monomers and solvents in the polymerization.

Investigation of Polymer Molecular Weight Distribution. To determine whether the unusual distribution is unique to 2,6-tBuAntN, we performed a monomer screening study using Pd(Mes) as the catalyst, which produced bimodal M_n distributions with 2,6-tBuAntN (Figure S5a). Among the substituted norbornenes examined (Figure 7), those with coordinating substituents such as carboxylic acid (N1), nitrile (N2), and carbonyl groups (N3) did not give detectable polymerization. The alcohol-substituted norbornene N4 was tolerated, although the polymerization rate was much slower than that of monomers with no heteroatoms (N5 and N6), which developed precipitates within the first hour of polymerization. The tolerance of hydroxyl groups is consistent with the prior literature which utilized this class of Pd catalysts in emulsion polymerizations.⁴⁹ This polymer of **N4** (I-N4) was characterized by GPC using DMF as the eluent and displayed a unimodal molecular weight distribution (Figure S8a).

Scheme 3. Two Probable Pathways of Resulting in Cross-Linked Polymers through Revealing a Branch Point; (a) Steric Congestion around Neighboring Repeating Units Inducing Cycloreversion and (b) Pd-Induced Cycloreversion through Cation $-\pi$ Interactions with a Phenyl Group^a

^aL represents generic ligands.

N5 produced a THF insoluble polymer that likely has significant cross-linking via the primary alkene. The ethylidene norbornene N6 was previously reported as a well-behaved monomer, ⁴⁹ and our resulting material (I-N6) also showed a unimodal GPC chromatogram in THF (Figure S8b). The small shoulder at 14 min for this material may be a result of small amount of cross-linking induced by the less reactive exocyclic double bond. We therefore conclude that the bimodal distribution is not caused by the catalyst but rather is unique to 2,6-tBuAntN.

To test monomer purity, we performed polymerizations with **2,6-tBuAntN** that was recrystallized twice, first from hexanes and then from acetone. The ¹H NMR of the resulting material showed no detectable impurities, suggesting that no species (e.g., norbornadiene) that can lead to cross-linking are present. Nonetheless, the bimodal distribution was still observed using **Pd(DMA)** and DCM as the solvent (Figure 8), making it unlikely that impurities are the cause of the bimodal distribution.

When **2,7-tBuAntN** was used as the monomer and polymerized with Pd(DMA), some high molecular weight material is clearly visible in the GPC as a shoulder at lower elution times (\approx 15 min, Figure S6), although it accounts for 40% of the total integrated area (72 h) as opposed to 50% with **2,6-tBuAntN** (Figure S5b). Based on this result, we suspect that the distribution of the *tert*-butyl substituents may play a role in the formation of the high molecular weight fraction.

The DCM for the polymerization reactions was used as purchased, and we considered the possibility that the added amylene stabilizer might be responsible for the high molecular weight peak when polymerizing **2,6-tBuAntN**. However, using d_2 -DCM that does not contain any stabilizers (DLM-23-10 \times 0.5 from Cambridge Isotope Laboratories) in place of DCM did not give any improvement in the chromatogram distribution. When the monomer and catalyst were dissolved separately in DCM and the monomer solution was added slowly to the catalyst solution, the high molecular weight signal at 13.5 min is suppressed, and the predominant polymer population displays

lower molecular weight. We performed this last experiment to determine if a slower rate of monomer dissolution might be causing the higher molecular weight species. As **2,7-tBuAntN** has a higher solubility than **2,6-tBuAntN** in DCM, this may explain why the former did not form significant amounts of high molecular weight material in the large-scale polymerization (Figure S11b).

Interestingly, using CHCl₃ as the solvent during polymerization resulted in the complete disappearance of the high molecular weight signal and only the low molecular weight material was observed in the GPC chromatogram (Figure 8a). The overall polymerization rate was also reduced, and low molecular weight material produced after 4 h in DCM had an equivalent molecular weight to the polymer produced after 28 h in CHCl₃.

Using either bromochloromethane (CH₂BrCl) or dibromomethane (DBM) as the polymerization solvent also resulted in the absence of high molecular weight material (Figure 8b), although a weak peak between 15 and 18 min suggests that some high molecular weight population is developing in DBM after 4 h of polymerization. Using dichlorobenzene (oDCB) also resulted in a partial suppression of high molecular weight material at t=16 min, similar to the DCM case with slow monomer addition.

After 28 h, all reaction solvents had polymerizations with shorter GPC elution times, suggesting increased degree of polymerization (Figure S9). Qualitatively, most chromatograms had similar profiles, but a strong RID (refractive index) signal at 15 min is now visible for oDCB, suggesting the presence of a high molecular weight species similar to the case with DCM as the reaction solvent.

Among the variables examined, the bimodal distribution seems to be highly specific to a combination of monomer (2,6-tBuAntN), catalyst (Pd(DMA) or Pd(Mes)), and solvent (DCM or oDCB). Other alterations of reaction parameters lead to the suppression of the high molecular weight GPC peak. We conducted GPC of the crude polymerization product with CHCl₃ rather than THF as the solvent and still observed two

Scheme 4. ROMP Reactions of (a) 2,6-tBuAntN and (b) 2,6-AdaAntN to Give R-2,6-tBuAntN and R-2,6-AdaAntN, Respectively

^aThe structure of Grubbs G3 is shown in the enclosed area.

clearly discernible peaks (Figure S10), showing that the unusual chromatogram is likely independent of the GPC solvent.

The large differences in apparent molecular weights allowed for selective extraction of the low $M_{\rm n}$ polymer from 2,6-tBuAntN by Soxhlet extraction with hexanes (Figure S11a). To investigate whether the remaining high molecular weight material was an aggregate, we compared its THF GPC chromatogram with and without first dissolving it in CHCl₃ at room temperature; both traces appeared to be effectively identical (Figure S11c). However, heating the thimble residue at 50 °C in CHCl₃ overnight resulted in an increase in the GPC signal from low molecular weight species at 22 min (Figure S11d). This suggests that either (1) there is aggregation and equilibration between the high and the low molecular species that only occurs upon heating or (2) a more polarizable solvent than hexanes/THF is required to release low molecular weight material trapped within the high molecular weight matrix.

Dynamic light scattering (DLS) was also used to check whether aggregation was responsible for the high molecular weight signal (Figure S12). In DCM, the polymer fraction extracted with hexanes was fit to a hydrodynamic radius of 4 nm, and the apparent high $M_{\rm n}$ residue had a hydrodynamic radius of 10 nm. DLS of the crude polymerization material is best fit to a bimodal distribution with highest fractions at hydrodynamic radii of approximately 3.5 and 30 nm, consistent with a mixture of low and high molecular weight material. Therefore, both species should be soluble, and we believe that aggregation is an unlikely explanation for the high molecular signal measured. We also found that filtration through 0.22 or 5 μ m syringe filters did not affect the bimodal distribution.

All factors considered, the most probable explanation for our bimodal molecular weight distribution is a small amount of cross-linking during the polymerization. The relatively well-defined chromatogram signals and relatively low PDI of the two populations suggest that any cross-linking happens in a controlled manner. Considering that Diels—Alder reactions can be reversible, we suggest that either (1) steric congestion between neighboring repeating units induced a retro Diels—Alder reaction or (2) perhaps the cationic Pd catalyst can have a cation— π interaction with one pendant phenyl group on the

monomer and facilitate a retro Diels—Alder reaction (Scheme 3). In either case, a small amount of this reaction would produce a norbornene group in the polymer chain and allow for a cross-link (branch) point. The amount of norbornyl units in the polymer is below NMR detection limits, and hence we presently can only speculate about the origins of the proposed cross-linking.

Comparison of ROMP Materials. To verify our assertions that an intact norbornyl system promotes free volume, we have synthesized ROMP polymers that are compositionally equivalent in terms of C/H but have a ring opened structure as shown in Scheme 4. We polymerized both 2,6-tBuAntN and 2,6-AdaAntN using Grubb's third generation catalyst to obtain the ring opened polymers R-2,6-tBuAntN and R-2,6-AdaAntN. Both polymerizations proceeded well, and Table 3 summarizes

Table 3. GPC Parameters of ROMP Polymer Using 2,6-tBuAntN and 2,6-AdaAntN as Monomers^a

	$M_{ m n}$	$M_{ m w}$	PDI
R-2,6-tBuAntN	1.65×10^{5}	1.71×10^{5}	1.04
R-2,6-AdaAntN	1.80×10^{5}	1.87×10^{5}	1.04

[&]quot;A bimodal distribution was observed, with a lower molecular weight population having $M_n=5.05\times 10^4$, $M_w=5.17\times 10^4$ and PDI = 1.02.

their GPC characterization. Considering their similar GPC traces (Figure S13) as well as $M_{\rm n}$ and $M_{\rm w}$ values of the two different polymers, we believe that the bulky adamantyl substituent did not significantly affect the monomer's propensity to under ROMP. This is in contrast to the insertion polymerization outlined earlier, where both 2,6 and 2,7-AdaAntN isomers did not undergo significant degree of polymerization with Pd(DMA). This is consistent with the fact that ROMP polymers have a more flexible and open structure that provides better access to the active metal catalytic center, thereby allowing for facile chain propagation.

Interestingly, both chromatograms showed a small shoulder at 16 min, which was reminiscent of the chromatogram of **N6**. Assuming that this is also a result of cross-linking, it necessitates the formation of a second alkene in the polymer backbone which is only achievable if retro Diels—Alder reactions occur. The

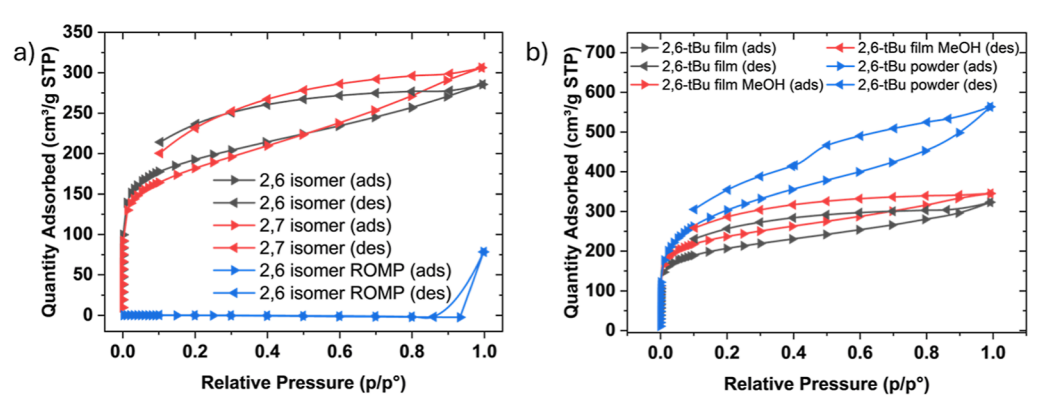


Figure 9. N₂ (77 K) BET comparisons of (a) **tBuAntN** insertion vs ROMP-based polymer films with MeOH treatment and (b) different treatments of **I-2,6-tBuAntN**.

Table 4. BET Parameters for Synthesized Polymers

entry	polymer ^a	N_2 BET area $(m^2 g^{-1})^b$	cumulative pore volume $(cm^3 g^{-1})^c$	pore width at maximum $dV/dW (A)^d$	micropore volume $(cm^3 g^{-1})^e$	mesopore volume $(cm^3 g^{-1})^e$
1	I-2,6-tBuAntN (film)	754	0.412	8.7	0.248	0.164
2	I-2,6-tBuAntN (MeOH- treated film)	871	0.495	6.8	0.296	0.199
3	I-2,6-tBuAntN (powder)	1086	0.815	6.8	0.328	0.487
4	I-2,7-tBuAntN (MeOH- treated film)	867	0.534	6.8	0.284	0.250
5	R-2,6-tBuAntN (powder)	322	0.531	10.5	0.0980	0.433
6	R-2,6-AdaAntN (powder)	479	0.466	14.8	0.144	0.322

^aFor I-2,6-tBuAntN and I-2,7-tBuAntN, measurements were conducted on the residue after removing lower molecular weight material through Soxhlet extraction with hexanes. ^bRouquerol transformation was performed on data before surface area estimation. ^cA slit geometry was assumed and an NLDFT model was used (see the Supporting Information). ^ddV/dW is obtained as the first derivative of cumulative pore volume against pore width. ^eMicropores have widths of <2 nm, while mesopores have widths with range 2–50 nm.

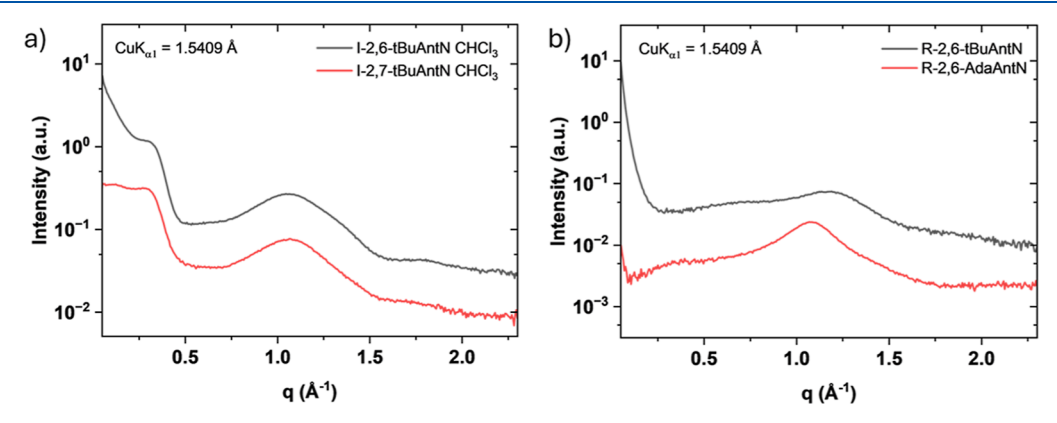


Figure 10. WAXS diffractograms of (a) insertion-based I-2,6- and I-2,7-tBuAntN and (b) ROMP-based R-2,6-tBuAntN and R-2,6-AdaAntN.

secondary peak at 20 min (Figure S13b) that is absent for R-2,6-tBuAntN may indicate a polymeric species after cycloreversion, but not cross-linking. We suggest that this species is absent for R-2,6-tBuAntN as the bulkier adamantyl substituents could provide a stronger driving force for cycloreversion compared with *tert*-butyl groups.

Surface Area Determination and Porosity. N₂ BET measurements at 77 K were performed to measure the surface areas of our materials. Different samples were prepared under three conditions: (1) film cast from slow evaporation of CHCl₃ solutions, (2) CHCl₃ cast film treated with MeOH overnight and then dried, and (3) dried powder collected via vacuum filtration after precipitating a CHCl₃ polymer solution into MeOH. Regardless of the MeOH treatments, the ROMP thin-film materials display negligible porosity (Figures 9a and S2).

This supports our central hypothesis that preserving both [2.2.1] and [2.2.2] bicyclic structures in the insertion polymerization is key to maintaining the highest intrinsic porosity. Both I-2,6- and I-2,7-tBuAntN with similar molecular weights gave similar surface areas, suggesting that the substitution pattern is unimportant for the porosity (Figure 9a). Thin-film measurements on solution cast I-2,6-tBuAntN revealed that MeOH treatment resulted in 15% higher surface area, presumably as a result of the removal of trapped CHCl₃ molecules through polymer swelling (Figure 9b). The ROMP materials did not benefit from MeOH soaking, and the low surface areas are the result of the more flexible backbones that allow for more efficient packing.

Powdered morphologies have a significant effect on measured BET surface areas (Figure 9b). All powders exhibited

approximately an additional 200 m² g⁻¹ of area compared to when cast into films, and this was also applicable to the ROMP polymers (Figure S2). Interestingly, the desorption curve of powdered I-2,6-tBuAntN displayed a H2-type hysteresis as defined by the IUPAC, ⁵⁹ which was also observed for I-AntN (Figure S1). This characteristic is reported to indicate a mesoporous character and indicates the presence of bottleneck-type pores within the polymer. ⁶¹ This type of hysteresis has been seen in cross-linked triptycene-based polymers ⁶³⁻⁶⁵ and similar norbornene insertion polymers. ⁴⁸

Performing pore size fitting on the BET isotherm data reveals that the ROMP polymers have two distinct pore size regimes at approximately 10 and 100 Å, while the two pore size regimes in insertion polymers are much more similar in size, centered around 7 and 12 Å. I-2,6-tBuAntN that was treated with MeOH also showed a reduction in the pore size from 8 to 6 Å (Figure S3 and Table 4 entries 1 and 2).

Measuring the WAXS diffractograms of our synthesized polymers gives us insights into their subnanometer structures. All polymers showed uniform halos in their two-dimensional pattern, consistent with being an amorphous material (Figure S15). Comparing the diffractograms of our synthesized I-AntN and I-N6 with that reported in that literature, peaks at similar q values are present in their WAXS profiles (Figure S16a and Table S2). I-2,6-tBuAntN and I-2,7-tBuAntN also shared similar profiles with two peaks, suggesting that similar polymers are obtained even with different substitution patterns on the monomers (Figure 10a and Table 5). The diffraction patterns do

Table 5. q Values and Corresponding Distances of I-2,6-tBuAntN, I-2,7-tBuAntN, R-2,6-tBuAntN, and R-2,6-AdaAntN Obtained from WAXS

	$q_1 (\mathring{A}^{-1})$	d_1 (Å) ^a	$q_2 (\mathring{A}^{-1})$	$d_2 (Å)^a$
I-2,6-tBuAntN	0.317	19.8	1.06	5.94
I-2,7-tBuAntN	0.305	20.6	1.07	5.87
R-2,6-tBuAntN			1.20	3.19
R-2,6-AdaAntN			1.08	5.80
$^{a}d=q/2\pi.$				

not seem to be strongly dependent on the polymer molecular weight (Figure S16b). Peaks at lower q values are attributed to distances between polymer chains, while larger q values are attributed to intrachain distances. ^{48,66}

Notably, R-2,6-tBuAntN and R-2,6-AdaAntN had a scattering profile with only one major peak at higher q values,

indicative of a different subnanometer structure compared to insertion-type polymers (Figure 10b). The absence of a peak at low q values is consistent with ROMP polymers having more flexible structures and tighter packing. The bulkier adamantyl substituent in R-2,6-AdaAntN increases the distance within chains compared to R-2,6-tBuAntN, indicated by the former polymer's lower q_2 value (1.08 vs 1.20 Å⁻¹). Overall, WAXS analysis supports our hypothesis that insertion-based polymerization gives material with high porosity and is anticipated to have better methane affinity.

Thermogravimetric analysis (TGA) measurement of **I-2,6**+**tBuAntN** showed that it has a T_{95} value around 321 °C (Figure 11a), which is slightly higher than that of **I-AntN** (300 °C) synthesized using **Pd(Dipp)**. A literature T_{95} value of 316 °C in argon for **I-AntN** synthesized using a nickel-based catalyst has been reported recently. Ecompared to **I-2,6**-tBuAntN, R-2,6-tBuAntN had a lower T_{95} value (303 °C) which may be due to its more flexible structure. R-2,6-AdaAntN had an improved T_{95} of 347 °C, suggesting that using adamantyl substituents increased the thermal stability even though the polymer backbone still has a flexible structure.

We also performed differential scanning calorimetry (DSC) measurements on I-2,6-tBuAntN, R-2,6-tBuAntN, and R-2,6-AdaAntN and in accord with literature studies, we did not detect any evidence of glass transition temperatures (T_g) below their T_{95} values (Figure S14).

We conducted variable-temperature (VT) ¹³C NMR to gather further evidence supporting the rigidity of the insertion polymer. Using **I-2,6-tBuAntN**, we acquired its spectra at 60 and 95 °C in solution and 25 °C in the solid state. The solution spectra are qualitatively identical to that of the solid state, and there is no obvious peak sharpening with increasing temperature (Figure 11b). This is consistent with a severely restricted backbone wherein there is no free rotation about bonds.

Comparing the ¹³C spectra of **I-2,6-tBuAntN** and **R-2,6-tBuAntN**, the latter polymer had an additional peak at 133 ppm (Figure 12a) attributable to an alkene unit that was absent in the former, again supporting insertion polymerization using the Pdbased catalysts. The sharper solution-state ¹³C and ¹H NMR signals of **R-2,6-tBuAntN** product compared to **I-2,6-tBuAntN** (Figure 12b) are also consistent with the former having a more flexible structure due to the ring opening of the rigid [2.2.1] norbornyl ring. The broad ¹H NMR spectra of insertion-polymerized norbornenes have also been observed in the literature. ^{48,49}

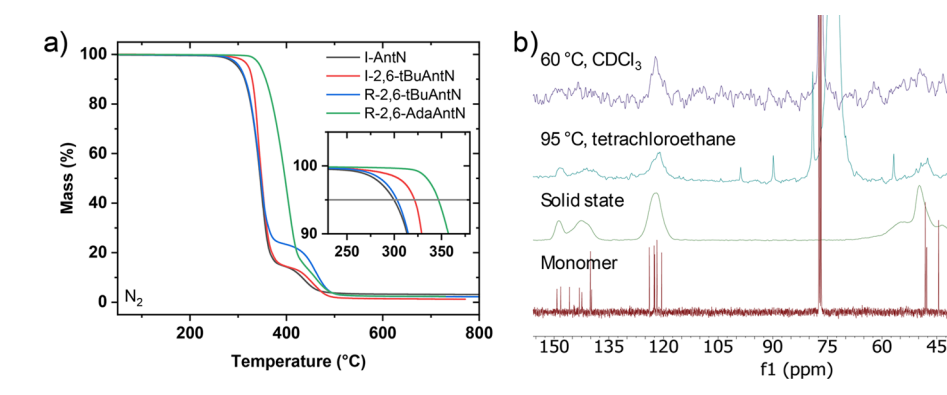


Figure 11. (a) N₂ TGA comparison between I-AntN, I-2,6-tBuAntN, R-2,6-tBuAntN, and R-2,6-AdaAntN. The horizontal line in the inset corresponds to 95% mass remaining. (b) VT ¹³C NMR measurements on I-2,6-tBuAntN.

15

30

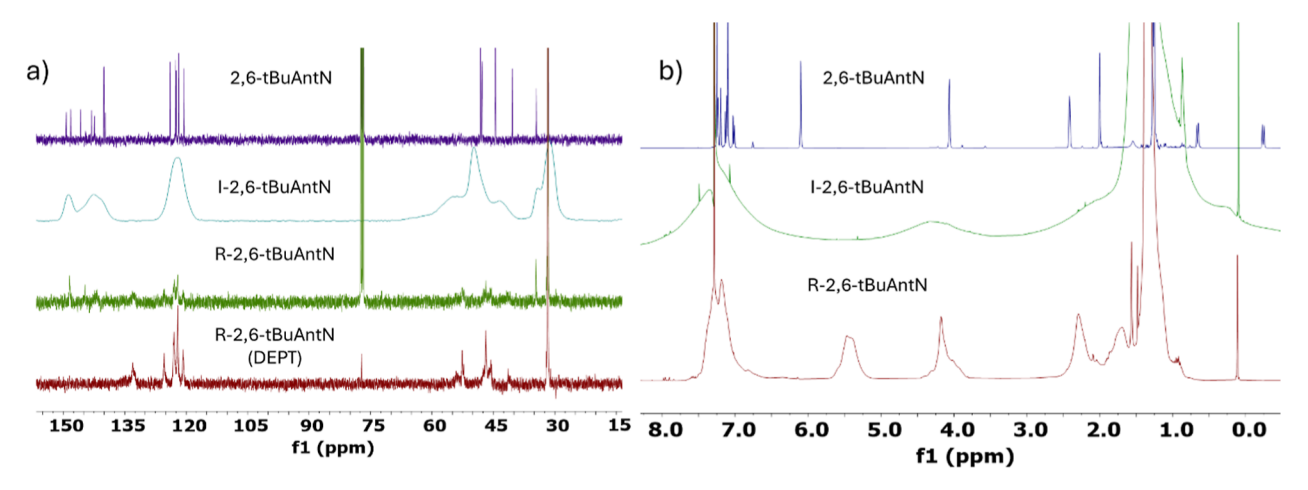


Figure 12. NMR comparison between insertion-type polymerization vs ROMP of 2,6-tBuAntN in CDCl₃. (a) ¹³C spectra and (b) ¹H spectra.

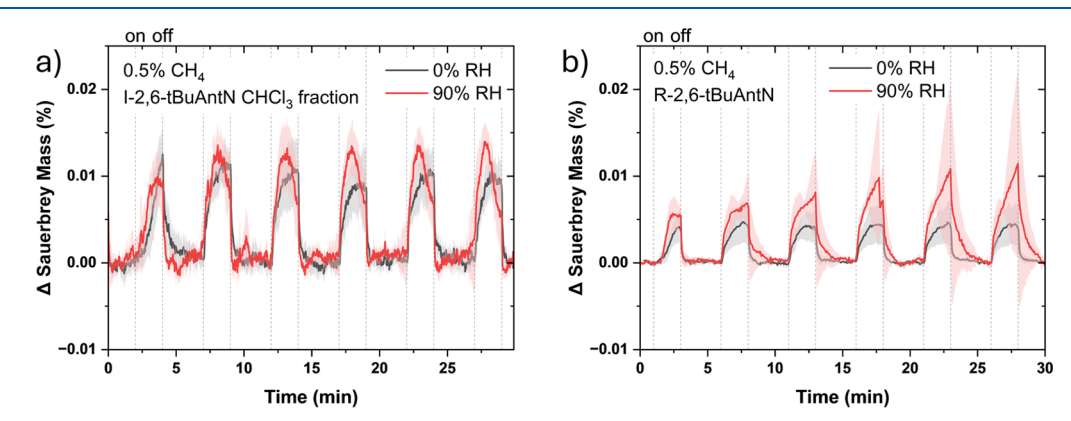


Figure 13. Percentage change in the Sauerbrey mass of (a) I-2,6-tBuAntN and (b) R-2,6-tBuAntN when exposed to 0.5% CH₄ at 0 and 90% RH. Baseline correction was performed on all traces. Shaded area around traces represents one standard deviation from the mean.

Affinity for Methane. We quantified the affinity of our synthesized polymers for methane absorption using a QCM with dissipation (QCM-D). Initial optimization of spin-coating conditions points to an optimal coating thickness of approximately 300 nm, as quantified by a cross-sectional analysis using scanning electron microscopy (Figure S17). Imaging was performed on a film both with and without MeOH treatment, and the resulting thickness increase from approximately 200 to 300 nm is consistent with MeOH swelling of the coatings. The additional porosity is corroborated by QCM measurements, where the films that has not received MeOH treatment displayed a reduced response to 5000 ppm (0.5%) CH₄ exposure at 0% relative humidity (RH) at room temperature.

The MeOH treatment also increased the QCM measurement consistency at high (90%) humidity levels across different resonant frequencies and dissipations. As seen in Figure S18, an untreated device exhibited irregular responses over a 0 to 90% RH range, when exposed to 0.5% methane. However, uniform responses are achieved after MeOH treatment over the entire RH range. It is noteworthy to mention that neither the MeOH treatment nor the RH levels significantly affected the dissipation values during methane exposure. In fact, exposure of a clean, uncoated crystal to $\mathrm{CH_4}$ at either humidity level also gave similar changes in dissipation values. Usually, an adsorption event is reflected as a decrease in resonant frequency, as well as a corresponding increase in dissipation due to the formation of a viscoelastic layer above the crystal that increases damping. A decrease in dissipation values during methane exposure could

suggest that the coating material increases in rigidity upon adsorbing methane. Changes in resonance frequencies may be converted to changes in mass adsorption using the Sauerbrey model. The absence of any dissipation is consistent with a very rigid polymer structure.

Under optimized spin-coating conditions, the high molecular weight fraction of **I-2,6-tBuAntN** isolated during Soxhlet extraction exhibited a positive change in Sauerbrey mass toward 0.5% CH₄ exposure under both dry and humid conditions (Figure 13a). As such, the material has an affinity for CH₄ adsorption that is largely independent of changes in humidity levels.

R-2,6-tBuAntN demonstrated a similar response to 0.5% CH₄ after spin coating. It demonstrated positive changes in Sauerbrey mass during CH₄ exposure at both 0 and 90% RH. However, response under humid conditions was less consistent than I-2,6-tBuAntN (Figure 13b) as seen from the larger standard deviation within the data. Figure S19 shows changes in Sauerbrey mass in ng cm⁻² before conversion to %. Comparing Figure S19b,d, the data before baseline correction at 90% RH for R-2,6-tBuAntN showed a more dramatic change than that for I-2,6-tBuAntN, which could also be consistent with the ROMP structure being more affected by water. Each exposure appears to consist of three time periods: (a) an initial increase in mass at the start of exposure, (b) subsequent slower mass uptake for the rest of the exposure, and (c) rapid decrease in mass when exposure stops and equilibration to the baseline.

We propose that under humid conditions, noncompetitive adsorption of CH_4 occurs within the material during the initial period (a), increasing the adsorbed mass. Eventually, competitive adsorption between CH_4 and H_2O occurs during the second period (b), where CH_4 displaces H_2O on the adsorption sites. As CH_4 has a density lower than that of H_2O vapor, this results in an apparent decrease in mass. During recovery time period (c), CH_4 first escapes the polymer matrix, corresponding to the rapid mass decrease. H_2O vapor then equilibrates throughout the material, leading to a rise in mass during baseline recovery.

The lower $M_{\rm n}$ materials, the hexane soluble Soxhlet extract of **I-2,6-tBuAntN** and the CHCl₃ soluble **I-2,7-tBuAntN**, were also evaluated for methane absorption by QCM. These materials have comparable degrees of polymerization with THF GPC $M_{\rm n}$ values of 1.80×10^4 and 5.65×10^4 , respectively. N₂ BET adsorption isotherms of these two materials as MeOH films show that the former has a reduced surface area compared with the latter, consistent with the trend in molecular weights (Figure S4).

These two materials behaved similarly when exposed to 0.5% ${\rm CH_4}$ (Figure S20). Under dry conditions (0% RH), we observed an uptake in Sauerbrey mass, consistent with the adsorption of methane. However, when we repeated the exposure under humid conditions (90% RH), we observed an apparent decrease in Sauerbrey mass. This may be due to the lower molecular weight material having a sufficiently flexible structure such that increased humidity triggers enough conformation change to detach the polymer film from the quartz crystal substrate. As a result, lower-molecular-weight materials are less useful for methane adsorption.

CONCLUSIONS

In summary, we have performed insertion polymerizations on substituted norbornenes and identified two preferred Pd-based polymerization catalysts. Through our optimization efforts, we determined that Pd(DMA) was the ideal catalyst and 2,6-tBuAntN gave the best balance between processability and high molecular weight. An unusual bimodal distribution was formed during polymerization, and our investigation into this phenomenon suggests that it is unique to 2,6-tBuAntN and is strongly influenced by solvent choice. Our best hypothesis to the bimodal nature of the molecular weight distribution is a cross-linking/branching process, made possible by a Diels—Alder cycloreversion to unveil a reactive norbornene within the polymer backbone.

For comparative studies, we synthesized **R-2,6-tBuAntN** and **R-2,6-AdaAntN** using ROMP to confirm the importance of the [2.2.1] bicyclic structures in promoting intrinsic free volume and microporosity, which assist in well-behaved reversible CH₄ adsorption over 0–90% RH. VT ¹H and ¹³C NMR results suggest that **I-2,6-tBuAntN** has an extremely rigid structure.

The polymers synthesized had morphology-dependent N_2 BET surface areas. Powdered samples produced by precipitation in MeOH displayed the highest BET values, followed by those from MeOH-treated thin films. Solution cast untreated films displayed the lowest surface areas. Preserving the [2.2.1] bicyclic norbornyl unit was important for maintaining the highest porosity levels, as both R-2,6-tBuAntN and R-2,6-AdaAntN did not show appreciable surface areas as films and a much lower surface area as powders when compared to I-2,6-tBuAntN. WAXS analysis suggests that insertion polymers generally had distances between and within chains larger than those of their

corresponding ROMP counterparts, consistent with a higher porosity. Lastly, both high molecular weight fraction of I-2,6-tBuAntN and R-2,6-tBuAntN had appreciable affinity for methane as demonstrated by QCM studies, but the former had better consistency at high humidity levels. This suggests that I-2,6-tBuAntN has the potential to function as a preconcentrator in methane-sensing applications.

ASSOCIATED CONTENT

5 Supporting Information

The Supporting Information is available free of charge at https://pubs.acs.org/doi/10.1021/acs.macromol.4c00972.

BET analysis, GPC chromatograms and DLS, polymerization in ethereal solvents, DSC, WAXS, QCM, general considerations, monomer synthesis, catalyst synthesis, polymerization reactions, kinetics study on polymerization reactions, general polymerization of N1 through N6, general polymerization of 2,6-tBuAntN using different solvents, X-ray crystallography, and references (PDF)

Single-crystal structures may be accessed on the Cambridge Crystallographic Database using deposition nos. 2343169 (Pd(DMA)), 2343170 (Pd(Xyl)), 2343171 (2,6-tBuAntN), 2343172 (2,7-tBuAntN), 2343173 (2,6-AdaAntN), and 2343174 (2,7-AdaAntN).

AUTHOR INFORMATION

Corresponding Author

Timothy M. Swager — Department of Chemistry and Institute for Soldier Nanotechnologies, Massachusetts Institute of Technology, Cambridge, Massachusetts 02139, United States; orcid.org/0000-0002-3577-0510; Email: tswager@mit.edu

Authors

Haosheng Feng — Department of Chemistry and Institute for Soldier Nanotechnologies, Massachusetts Institute of Technology, Cambridge, Massachusetts 02139, United States; orcid.org/0000-0003-1031-7733

Shao-Xiong Lennon Luo — Department of Chemistry and Institute for Soldier Nanotechnologies, Massachusetts Institute of Technology, Cambridge, Massachusetts 02139, United States; orcid.org/0000-0001-5308-4576

Complete contact information is available at: https://pubs.acs.org/10.1021/acs.macromol.4c00972

Author Contributions

Haosheng Feng: Investigation, methodology, and writing—original draft, review, and editing. Shao-Xiong Lennon Luo: Investigation—catalyst synthesis and writing—review and editing. Timothy M. Swager: Conceptualization, funding acquisition, supervision, and writing—review and editing.

Funding

This project received funding from the Department of Energy Advanced Research Projects Agency-Energy (ARPA-E) under the Reducing Methane Emissions Every Day of the Year (REMEDY) program and The National Science Foundation (DMR-2207299).

Notes

The authors declare no competing financial interest.

ACKNOWLEDGMENTS

We thank Dr. Peter Muller's services for data acquisition, structure solution, and refinement of single crystals. This research benefitted from facilities and equipment made available by the Institute for Soldier Nanotechnologies, a U.S. Armysponsored UARC at MIT.

REFERENCES

- (1) Whiticar, M. J. A Geochemial Perspective of Natural Gas and Atmospheric Methane. *Org. Geochem.* **1990**, *16* (1–3), 531–547.
- (2) Hassan, A.; Ilyas, S. Z.; Jalil, A.; Ullah, Z. Monetization of the Environmental Damage Caused by Fossil Fuels. *Environ. Sci. Pollut. Res.* **2021**, 28 (17), 21204–21211.
- (3) Paraschiv, S.; Paraschiv, L. S. Trends of Carbon Dioxide (CO₂) Emissions from Fossil Fuels Combustion (Coal, Gas and Oil) in the EU Member States from 1960 to 2018. *Energy Rep* **2020**, *6*, 237–242.
- (4) Valiulin, S. V.; Onischuk, A. A.; Baklanov, A. M.; Bazhina, A. A.; Paleev, D. Yu.; Zamashchikov, V. V.; Korzhavin, A. A.; Dubtsov, S. N. Effect of Coal Mine Organic Aerosol on the Methane/Air Lower Explosive Limit. *Int. J. Coal Sci. Technol.* **2020**, 7 (4), 778–786.
- (5) The Earth's Energy Budget. Climate Feedbacks and Climate Sensitivity. Climate Change 2021—the Physical Science Basis: Working Group I Contribution to the Sixth Assessment Report of the Intergovernmental Panel on Climate Change; Intergovernmental Panel on Climate Change (IPCC); Cambridge University Press: Cambridge, 2023; pp 923–1054.
- (6) Vogel, E.; Dalheimer, B.; Beber, C. L.; de Mori, C.; Palhares, J. C. P.; Novo, A. L. M. Environmental Efficiency and Methane Abatement Costs of Dairy Farms from Minas Gerais, Brazil. *Food Policy* **2023**, *119*, 102520.
- (7) Olczak, M.; Piebalgs, A.; Balcombe, P. A Global Review of Methane Policies Reveals That Only 13% of Emissions Are Covered with Unclear Effectiveness. *One Earth* **2023**, *6* (5), 519–535.
- (8) Dobson, S.; Goodday, V.; Winter, J. If It Matters, Measure It: A Review of Methane Sources and Mitigation Policy in Canada. *Int. Rev. Environ. Resour. Econ.* **2023**, *16* (3–4), 309–429.
- (9) Sawyer, W.; Genina, I.; Brenneis, R.; Feng, H.; Li, Y.; Luo, S.-X. L. Methane Emissions and Global Warming: Mitigationtechnologies, Policy Ambitions, and Global Efforts. *MIT Sci. Policy Rev.* **2022**, *3*, 73–84
- (10) de Gouw, J. A.; Veefkind, J. P.; Roosenbrand, E.; Dix, B.; Lin, J. C.; Landgraf, J.; Levelt, P. F. Daily Satellite Observations of Methane from Oil and Gas Production Regions in the United States. *Sci. Rep.* **2020**, *10* (1), 1379.
- (11) Palmer, P. I.; Feng, L.; Lunt, M. F.; Parker, R. J.; Bösch, H.; Lan, X.; Lorente, A.; Borsdorff, T. The Added Value of Satellite Observations of Methane Forunderstanding the Contemporary Methane Budget. *Philos. Trans. R. Soc. Math. Phys. Eng. Sci.* **2021**, 379 (2210), 20210106.
- (12) Bíró, F.; Dücső, C.; Radnóczi, G. Z.; Baji, Z.; Takács, M.; Bársony, I. ALD Nano-Catalyst for Micro-Calorimetric Detection of Hydrocarbons. Sens. Actuators B Chem. 2017, 247, 617–625.
- (13) Liu, X.; Cheng, B.; Hu, J.; Qin, H.; Jiang, M. Preparation, Structure, Resistance and Methane-Gas Sensing Properties of Nominal La1–xMgxFeO3. Sens. Actuators B Chem. 2008, 133 (1), 340–344.
- (14) Shaalan, N. M.; Rashad, M.; Moharram, A. H.; Abdel-Rahim, M. A. Promising Methane Gas Sensor Synthesized by Microwave-Assisted Co₃O₄ Nanoparticles. *Mater. Sci. Semicond. Process.* **2016**, *46*, 1–5.
- (15) Zhang, D.; Chang, H.; Li, P.; Liu, R. Characterization of Nickel Oxide Decorated-Reduced Graphene Oxide Nanocomposite and Its Sensing Properties toward Methane Gas Detection. *J. Mater. Sci. Mater. Electron.* **2016**, 27 (4), 3723–3730.
- (16) Wang, Z.; Guo, M.; Baker, G. A.; Stetter, J. R.; Lin, L.; Mason, A. J.; Zeng, X. Methane—Oxygen Electrochemical Coupling in an Ionic Liquid: A Robust Sensor for Simultaneous Quantification. *Analyst* **2014**, *139* (20), 5140–5147.

- (17) Yang, B.; Xu, J.; Wang, C.; Xiao, J. A Potentiometric Sensor Based on $SmMn_2O_5$ Sensing Electrode for Methane Detection. *Mater. Chem. Phys.* **2020**, 245, 122679.
- (18) Hong, T.; Culp, J. T.; Kim, K.-J.; Devkota, J.; Sun, C.; Ohodnicki, P. R. State-of-the-Art of Methane Sensing Materials: A Review and Perspectives. *TrAC Trends Anal. Chem.* **2020**, *125*, 115820.
- (19) Fu, L.; You, S.; Li, G.; Li, X.; Fan, Z. Application of Semiconductor Metal Oxide in Chemiresistive Methane Gas Sensor: Recent Developments and Future Perspectives. *Molecules* **2023**, 28 (18), 6710.
- (20) Aldhafeeri, T.; Tran, M.-K.; Vrolyk, R.; Pope, M.; Fowler, M. A Review of Methane Gas Detection Sensors: Recent Developments and Future Perspectives. *Inventions* **2020**, *5* (3), 28.
- (21) Li, H.; Wu, R.; Tian, X.; Han, L.; Chen, T.; Yang, B.; Zhi, Z.; Hua, Z.; Fan, S. A Catalytic Filter Based on Pt-CeO₂ for Selective Methane Detection with SnO₂ Sensors. *Sens. Actuators B Chem.* **2023**, 389, 133872.
- (22) Bezdek, M. J.; Luo, S.-X. L.; Ku, K. H.; Swager, T. M. A Chemiresistive Methane Sensor. *Proc. Natl. Acad. Sci. U.S.A.* **2021**, *118* (2), No. e2022515118.
- (23) Li, X.; Gao, Z.; Li, B.; Zhang, X.; Li, Y.; Sun, J. Self-Healing Superhydrophobic Conductive Coatings for Self-Cleaning and Humidity-Insensitive Hydrogen Sensors. *Chem. Eng. J.* **2021**, *410*, 128353
- (24) Qu, F.; Zhang, S.; Huang, C.; Guo, X.; Zhu, Y.; Thomas, T.; Guo, H.; Attfield, J. P.; Yang, M. Surface Functionalized Sensors for Humidity-Independent Gas Detection. *Angew. Chem., Int. Ed.* **2021**, *60* (12), 6561–6566.
- (25) Esmeryan, K. D.; Yordanov, T. A.; Vergov, L. G.; Raicheva, Z. G.; Radeva, E. I. Humidity Tolerant Organic Vapor Detection Using a Superhydrophobic Quartz Crystal Microbalance. *IEEE Sens. J.* **2015**, *15* (11), 6318–6325.
- (26) Leidinger, M.; Rieger, M.; Sauerwald, T.; Alépée, C.; Schütze, A. Integrated Pre-Concentrator Gas Sensor Microsystem for ppb Level Benzene Detection. *Sens. Actuators B Chem.* **2016**, 236, 988–996.
- (27) Chowdhury, A. R.; Lee, T.-A.; Day, C.; Hutter, T. A Review of Preconcentrator Materials, Flow Regimes and Detection Technologies for Gas Adsorption and Sensing. *Adv. Mater. Interfaces* **2022**, *9* (20), 2200632.
- (28) Chapala, P. P.; Bermeshev, M. V.; Starannikova, L. E.; Belov, N. A.; Ryzhikh, V. E.; Shantarovich, V. P.; Lakhtin, V. G.; Gavrilova, N. N.; Yampolskii, Y. P.; Finkelshtein, E. Sh. A Novel, Highly Gas-Permeable Polymer Representing a New Class of Silicon-Containing Polynorbornens As Efficient Membrane Materials. *Macromolecules* **2015**, 48 (22), 8055–8061.
- (29) Bermeshev, M. V.; Syromolotov, A. V.; Gringolts, M. L.; Starannikova, L. E.; Yampolskii, Y. P.; Finkelshtein, E. S. Synthesis of High Molecular Weight Poly[3-{tris(Trimethylsiloxy)Silyl}-tricyclononenes-7] and Their Gas Permeation Properties. *Macromolecules* **2011**, *44* (17), 6637–6640.
- (30) Swager, T. M. Iptycenes in the Design of High Performance Polymers. Acc. Chem. Res. 2008, 41 (9), 1181–1189.
- (31) Zhao, Y.; He, Y.; Swager, T. M. Porous Organic Polymers via Ring Opening Metathesis Polymerization. *ACS Macro Lett.* **2018**, *7* (3), 300–304.
- (32) Alentiev, D. A.; Bermeshev, M. V. Design and Synthesis of Porous Organic Polymeric Materials from Norbornene Derivatives. *Polym. Rev.* **2022**, *62* (2), 400–437.
- (33) Mehler, C.; Risse, W. Addition Polymerization of Norbornene Catalyzed by Palladium(2+) Compounds. A Polymerization Reaction with Rare Chain Transfer and Chain Termination. *Macromolecules* **1992**, 25 (16), 4226–4228.
- (34) Sen, A.; Lai, T.-W.; Thomas, R. R. Reactions of Electrophilic Transition Metal Cations with Olefins and Small Ring Compounds. Rearrangements and Polymerizations. *J. Organomet. Chem.* **1988**, 358 (1–3), 567–588.
- (35) Bermesheva, E. V.; Bermeshev, M. V. Single-Component Catalysts for the Vinyl-Addition Polymerization of Norbornene and Its Derivatives. *ChemCatChem* **2023**, *15* (24), No. e202300818.

- (36) Hsu, J. H.; Peltier, C. R.; Treichel, M.; Gaitor, J. C.; Li, Q.; Girbau, R.; Macbeth, A. J.; Abruña, H. D.; Noonan, K. J. T.; Coates, G. W.; Fors, B. P. Direct Insertion Polymerization of Ionic Monomers: Rapid Production of Anion Exchange Membranes. *Angew. Chem., Int. Ed.* **2023**, *62* (30), No. e202304778.
- (37) De Stefano, F.; Baur, M.; De Rosa, C.; Mecking, S. Keto-Polyethylenes with Controlled Crystallinity and Materials Properties from Catalytic Ethylene–CO–Norbornene Terpolymerization. *Macromolecules* **2024**, *57* (3), 1072–1079.
- (38) Wallace, K. C.; Schrock, R. R. Ring-Opening Polymerization of Norbornene by a Tantalum Catalyst: A Living Polymerization. *Macromolecules* **1987**, *20* (2), 448–450.
- (39) Bielawski, C. W.; Grubbs, R. H. Living Ring-Opening Metathesis Polymerization. *Prog. Polym. Sci.* **2007**, 32 (1), 1–29.
- (40) Schrock, R. R. Synthesis of Stereoregular Polymers through Ring-Opening Metathesis Polymerization. *Acc. Chem. Res.* **2014**, *47* (8), 2457–2466.
- (41) Miyasako, N.; Matsuoka, S.; Suzuki, M. Ring-Opening Metathesis Polymerization of Endo- and Exo-Norbornene Lactones. *Macromol. Rapid Commun.* **2021**, 42 (8), 2000326.
- (42) Lai, H. W. H.; Teo, Y. C.; Xia, Y. Functionalized Rigid Ladder Polymers from Catalytic Arene-Norbornene Annulation Polymerization. *ACS Macro Lett.* **2017**, *6* (12), 1357–1361.
- (43) Robinson, A. M.; Xia, Y. Regioisomeric Spirobifluorene CANAL Ladder Polymers and Their Gas Separation Performance. *ACS Macro Lett.* **2024**, *13*, 118–123.
- (44) Long, T. M.; Swager, T. M. Molecular Design of Free Volume as a Route to Low-κ Dielectric Materials. *J. Am. Chem. Soc.* **2003**, *125* (46), 14113–14119.
- (45) Crist, R. D.; Huang, Z.; Guo, R.; Galizia, M. Effect of Thermal Treatment on the Structure and Gas Transport Properties of a Triptycene-Based Polybenzoxazole Exhibiting Configurational Free Volume. J. Membr. Sci. 2020, 597, 117759.
- (46) Tsui, N. T.; Paraskos, A. J.; Torun, L.; Swager, T. M.; Thomas, E. L. Minimization of Internal Molecular Free Volume: A Mechanism for the Simultaneous Enhancement of Polymer Stiffness, Strength, and Ductility. *Macromolecules* **2006**, *39* (9), 3350–3358.
- (47) Hong, M.; Cui, L.; Liu, S.; Li, Y. Synthesis of Novel Cyclic Olefin Copolymer (COC) with High Performance via Effective Copolymerization of Ethylene with Bulky Cyclic Olefin. *Macromolecules* **2012**, 45 (13), 5397–5402.
- (48) Zotkin, M. A.; Alentiev, D. A.; Shorunov, S. V.; Sokolov, S. E.; Gavrilova, N. N.; Bermeshev, M. V. Microporous Polynorbornenes Bearing Carbocyclic Substituents: Structure-Property Study. *Polymer* **2023**, *269*, 125732.
- (49) Bermesheva, E. V.; Medentseva, E. I.; Khrychikova, A. P.; Wozniak, A. I.; Guseva, M. A.; Nazarov, I. V.; Morontsev, A. A.; Karpov, G. O.; Topchiy, M. A.; Asachenko, A. F.; Danshina, A. A.; Nelyubina, Y. V.; Bermeshev, M. V. Air-Stable Single-Component Pd-Catalysts for Vinyl-Addition Polymerization of Functionalized Norbornenes. *ACS Catal.* 2022, *12* (24), 15076–15090.
- (50) Bermesheva, E. V.; Wozniak, A. I.; Andreyanov, F. A.; Karpov, G. O.; Nechaev, M. S.; Asachenko, A. F.; Topchiy, M. A.; Melnikova, E. K.; Nelyubina, Y. V.; Gribanov, P. S.; Bermeshev, M. V. Polymerization of 5-Alkylidene-2-Norbornenes with Highly Active Pd—N-Heterocyclic Carbene Complex Catalysts: Catalyst Structure—Activity Relationships. *ACS Catal.* **2020**, *10* (3), 1663—1678.
- (51) Kuhn, K. M.; Grubbs, R. H. A Facile Preparation of Imidazolinium Chlorides. *Org. Lett.* **2008**, *10* (10), 2075–2077.
- (52) Stewart, I. C.; Ung, T.; Pletnev, A. A.; Berlin, J. M.; Grubbs, R. H.; Schrodi, Y. Highly Efficient Ruthenium Catalysts for the Formation of Tetrasubstituted Olefins via Ring-Closing Metathesis. *Org. Lett.* **2007**, 9 (8), 1589–1592.
- (53) Prozorovskii, A. E.; Tafeenko, V. A.; Ribakov, V. B.; Shokova, E. A.; Kovalev, V. V. Crystal and Molecular Structure of 2,6-Di(1-Adamantyl) Anthracene. *J. Struct. Chem.* 1987, 28 (1), 165–168.
- (54) Herron, N.; Guidry, M. a.; Rostovtsev, V.; North, V. J.; Merlo, J. a.; Dogra, K. Green Luminescent Materials. WO 2008150828 A2, December 11, 2008.

- (55) Boobalan, R.; Chein, R.-J. Oxathiaborolium-Catalyzed Enantioselective [4 + 2] Cycloaddition and Its Application in Lewis Acid Coordinated and Chiral Lewis Acid Catalyzed [4 + 2] Cycloaddition. *Org. Lett.* **2021**, 23 (17), 6760–6764.
- (\$6) Scerba, M. T.; Bloom, S.; Haselton, N.; Siegler, M.; Jaffe, J.; Lectka, T. Interaction of a C–F Bond with the π -System of a C=C Bond or "Head On" with a Proximate C–H Bond. *J. Org. Chem.* **2012**, 77 (3), 1605–1609.
- (57) Batsanov, A. S.; Hesselink, J. L. 2-Norbornene- Exo Cis -5,6-Dicarboxylic Acid. *Acta Crystallogr. Sect. E Struct. Rep. Online* **2002**, 58 (11), o1272-o1274.
- (58) Kodama, K.; Yamaguchi, S.; Hayano, S.; Houkawa, T.; Kitahara, Y.; Shitara, H.; Hirose, T. Characterization and Enantiomer Separation of Indene-Derived Hexacyclic Hydrocarbon and Its Application as a Chiral Source. *Tetrahedron* **2021**, *87*, 132082.
- (59) Thommes, M.; Kaneko, K.; Neimark, A. V.; Olivier, J. P.; Rodriguez-Reinoso, F.; Rouquerol, J.; Sing, K. S. W. Physisorption of Gases, with Special Reference to the Evaluation of Surface Area and Pore Size Distribution (IUPAC Technical Report). *Pure Appl. Chem.* **2015**, *87* (9–10), 1051–1069.
- (60) Errahali, M.; Gatti, G.; Tei, L.; Paul, G.; Rolla, G. A.; Canti, L.; Fraccarollo, A.; Cossi, M.; Comotti, A.; Sozzani, P.; Marchese, L. Microporous Hyper-Cross-Linked Aromatic Polymers Designed for Methane and Carbon Dioxide Adsorption. *J. Phys. Chem. C* **2014**, *118* (49), 28699–28710.
- (61) Nayak, N. B.; Nayak, B. B. Temperature-Mediated Phase Transformation, Pore Geometry and Pore Hysteresis Transformation of Borohydride Derived in-Born Porous Zirconium Hydroxide Nanopowders. *Sci. Rep.* **2016**, *6* (1), 26404.
- (62) Nguyen, P. T. M.; Fan, C.; Do, D. D.; Nicholson, D. On the Cavitation-Like Pore Blocking in Ink-Bottle Pore: Evolution of Hysteresis Loop with Neck Size. *J. Phys. Chem. C* **2013**, *117* (10), 5475–5484.
- (63) Ansari, M.; Bera, R.; Das, N. A Triptycene Derived Hyper-crosslinked Polymer for Gas Capture and Separation Applications. *J. Appl. Polym. Sci.* **2022**, *139* (1), 51449.
- (64) Zhang, C.; Zhu, P.-C.; Tan, L.; Liu, J.-M.; Tan, B.; Yang, X.-L.; Xu, H.-B. Triptycene-Based Hyper-Cross-Linked Polymer Sponge for Gas Storage and Water Treatment. *Macromolecules* **2015**, *48* (23), 8509–8514.
- (65) He, Y.; Bao, W.; Hua, Y.; Guo, Z.; Fu, X.; Na, B.; Yuan, D.; Peng, C.; Liu, H. Efficient Adsorption of Methyl Orange and Methyl Blue Dyes by a Novel Triptycene-Based Hyper-Crosslinked Porous Polymer. RSC Adv. 2022, 12 (9), 5587–5594.
- (66) Dujardin, W.; Van Goethem, C.; Steele, J. A.; Roeffaers, M.; Vankelecom, I. F. J.; Koeckelberghs, G. Polyvinylnorbornene Gas Separation Membranes. *Polymers* **2019**, *11* (4), 704.